Method for calculating electronic structures near surfaces of semi-infinite crystals

Yonas B. Abraham and N. A. W. Holzwarth*
Department of Physics, Wake Forest University, Winston-Salem, North Carolina 27109-7507, USA
(Received 25 August 2005; revised manuscript received 31 October 2005; published 6 January 2006)

We present a stable scheme to calculate continum and bound electronic states in the vicinity of a surface of a semi-infinite crystal within the framework of density functional theory. The method is designed for solution of the Kohn-Sham equations in a pseudpotential formulation, including both local and separable nonlocal contributions. The method is based on the Numerov integration algorithm and uses singular value decomposition to control the exponentially growing contributions. The method has been successfully tested on the Li (110) surface with and without adsorbed H. For this model system, we are able to locate the energies of H-induced surface states relative to the corresponding energies of bulk continum states. Results encourage further development.

DOI: 10.1103/PhysRevB.73.035412 PACS number(s): 73.20.At, 71.15.−m, 71.20.Dg

I. INTRODUCTION

In the large literature of surface simulations, the vast majority of results have been obtained using a supercell approach in the slab geometry. This approach has been successfully used to study ideal clean surfaces as well as surfaces with adsorbates as discussed in several review monographs and articles.[1–4] The supercell approach has even been used to model workfunction variations of a material near its facet edges[5,6] and has been recently adapted to model transport processes.[7]

In principle, all of these simulations of surfaces and interfaces could be formulated in terms of semi-infinite boundary-value problems which could have several advantages. First, in the semi-infinite formulation there is one mathematical boundary for each physical boundary, while in the slab formulation there is an extra mathematical boundary which may cause unphysical interference effects or spurious surface features in the results. Secondly, in the semi-infinite formulation, the full computational effort can be focused on the interface region itself using knowledge of the bulk contributions as input, while in the slab formulation the bulk is modeled by the interior layers of the slab. Thirdly, in the semi-infinite formulation it is possible to directly locate the surface states relative to the bulk band edges, while in a slab formulation, the distinction between bulk and surface effects is more complicated. In summary, the semi-infinite formulation of these surface and interface simulations more closely represents the physical systems and we expect it to result in new insights into surface physics which may not be so readily apparent in other approaches.

In contrast to surface simulations based on the slab formulation, there have been a relatively smaller number based on the semi-infinite formulation. For example, there is the pioneering work of Lang and Kohn[8,9] on the self-consistent jellium surface, later extended by Lang and Williams[10,11] to treat an atomic adsorbate on a jellium surface. Appelbaum and Hamman[12,13] developed a method based on a local pseudopotential formalism and on numerical integration of the Schrödinger equation in the surface region, matching to a linear combination of Bloch waves in the interior of the solid. In order to analyze energetic electrons in low energy electron emission[14–16] or in photoemission.[17,18] Green's function methods with muffin-tin potential models have been very successful. Stiles and Hamann[19] developed a method based on constructing a Green's function from generalized Bloch states in a linearize augmented plane wave (LAPW) basis for treating electron transmission through interfaces.[20] Other augmented plane wave schemes have recently been developed by several authors.[21–24] In order to self-consistently determine the electronic and structural ground state of semiconductor surfaces, Krüger and Pollmann developed a method based on a Green's functions expressed in a Gaussian basis.[25] This approach has been quite successful for studying the lattice relaxation and surface state structure of several semiconductor surfaces.[26,27] Interest in quantum transport has recently generated several new approaches to solving the semi-infinite boundary value problem.[28–32]

As revealed in this previous work, the numerical challenge of treating the semi-infinite boundary value problem is to control the exponentially growing solutions present in the differential equation in a planar representation. For example, in the work of Choi and Ihm,[28] the exponentially growing solutions were controlled with a rescaling process during the numerical integration. In the present work, we formulate a numerical scheme for solving the semi-infinite boundary value problem using singular value decomposition[33] to stabilize the solution. The formalism is presented in Sec. II with details in the Appendix. The method is used to analyze the ideal (110) surface of pure Li and Li with H adsorbed at a bridge site in Sec. III. In Sec. IV the formalism and results are further analyzed and summarized.

II. FORMALISM

A. Definition of the problem

The Kohn-Sham equations[34,35] for the systems of interest can be assumed to take the following general form:

$$\{\tilde{H}(\mathbf{r}) - E_\alpha\}|\tilde{\Psi}_\alpha(\mathbf{r})\rangle + \sum_{aij} |\tilde{p}_i^a\rangle\{D_{ij}^a - E_\alpha O_{ij}^a\}\langle\tilde{p}_j^a|\tilde{\Psi}_\alpha(\mathbf{r})\rangle = 0. \tag{1}$$

Here, the first term represents a local Hamiltonian including kinetic and potential contributions:

$$\tilde{H}(\mathbf{r}) = -\frac{\hbar^2}{2m}\nabla^2 + \tilde{v}(\mathbf{r}). \quad (2)$$

The coefficients D_{ij}^a and O_{ij}^a represent nonlocal Hamiltonian and overlap matrix elements, with a representing an atomic site index and i,j representing basis function indices $(n_i l_i m_i, n_j l_j m_j)$. In our work these coefficients are based on the projector augmented wave (PAW) formulation of Blöchl,[36–39] however, with trivial modification, they could also represent the soft-pseudopotential formulation of Vanderbilt[40] or the separable approximation for norm-conserving pseudopotentials of Kleinman and Bylander.[41] The localized functions $\tilde{p}_i^a(\mathbf{r}-\mathbf{R}^a)$ (called "projector" functions in the PAW formulation) are centered at atomic sites $\mathbf{R}^a$ and are confined within nonoverlapping spheres of radii r_c^a. The energy eigenvalue is denoted by E_α and the corresponding pseudo-wave function is denoted by $\tilde{\Psi}_\alpha(\mathbf{r})$.

For the surface geometry, we assume that there is periodicity within the surface plane, so that it will be convenient to represent the wave functions in two-dimensional plane wave expansion within each plane parallel to the surface and a discrete grid along the direction $(\hat{\mathbf{z}})$ normal to the surface. The general surface representation of the wave function takes the form[42]

$$\tilde{\Psi}_{\mu\kappa}(\mathbf{r}_\parallel, z) = \sqrt{\frac{1}{\mathcal{A}}}\sum_{\mathbf{g}} e^{i(\kappa+\mathbf{g})\cdot\mathbf{r}_\parallel} f_{\mu\kappa}(\mathbf{g}, z), \quad (3)$$

where $\mathcal{A}$ represents the area of the surface unit cell, κ and $\{\mathbf{g}\}$ represent the surface Bloch and reciprocal lattice vectors, respectively, and μ represents a band or surface state index. In practice, the summation over $\{\mathbf{g}\}$ is carried out over $N_\mathbf{g}$ surface reciprocal lattice vectors such that $|\kappa+\mathbf{g}| < G_{\text{cut}}$ where G_{cut} is chosen to control convergence. Our task is to determine the wave functions components $f_{\mu\kappa}(\mathbf{g}, z)$, which solve the Kohn-Sham equations for a given energy $E_{\mu\kappa}$ and satisfy the semi-infinite boundary conditions of the surface geometry. Explicitly, this means that $\tilde{\Psi}_{\mu\kappa}(\mathbf{r}_\parallel, z)$ represents a decaying or propagating wave function in the vacuum region of the surface (for $E_{\mu\kappa}$ below or above the workfunction of the material, respectively) and represents a linear combination of Bloch waves or decaying waves in the interior bulk region of the surface (for $E_{\mu\kappa}$within the ranges of the bulk bands or outside those ranges, respectively). For simplicity in notation, we will drop the $\mu\kappa$ indices. The main equations are presented below and the details are given in the Appendix.

The Kohn-Sham equations (1) for the surface geometry take the form:

$$\frac{d^2 f(\mathbf{g}, z)}{dz^2} = \sum_{\mathbf{g}'} \mathcal{V}_{\mathbf{g}\mathbf{g}'}(z) f(\mathbf{g}', z) + \sum_{ai} \bar{\tilde{p}}_i^a(\mathbf{g}, z)\mathcal{K}_i^a. \quad (4)$$

The first summation is carried out over $N_\mathbf{g}$ surface reciprocal lattice vectors as discussed above, with the local contribution defined according to

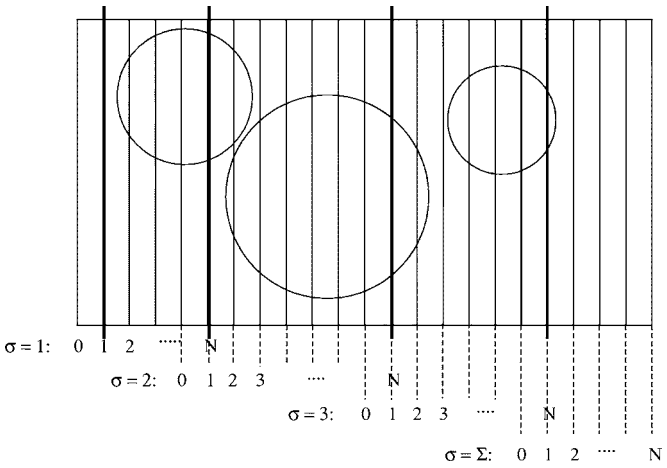

FIG. 1. Diagram showing discretized and partitioned z axis. Circles indicate cross sections of atomic spheres in the plane of the diagram.

$$\mathcal{V}_{\mathbf{g}\mathbf{g}'}(z) \equiv \left[|\kappa+\mathbf{g}|^2 - \frac{2m}{\hbar^2}E\right]\delta_{\mathbf{g}\mathbf{g}'} + \frac{2m}{\hbar^2}\bar{\tilde{v}}(\mathbf{g}-\mathbf{g}', z). \quad (5)$$

Here $\bar{\tilde{v}}(\mathbf{g}, z)$ is the two-dimensional Fourier transform of the local potential is defined in Eq. (A1). The second summation in Eq. (4) is carried out over site a and orbital i indices representing the nonlocal contributions as defined in terms of the two-dimensional Fourier transform of the projector function $\bar{\tilde{p}}_i^a(\mathbf{g}, z)$, given in Eqs. (A2)–(A4), and an integral coefficient of the form:

$$\mathcal{K}_i^a \equiv \sum_j \frac{2m}{\hbar^2}(D_{ij}^a - EO_{ij}^a)\langle\bar{\tilde{p}}_j^a|f\rangle, \quad (6)$$

where

$$\langle\bar{\tilde{p}}_i^a|f\rangle \equiv \sum_{\mathbf{g}} \int dz \bar{\tilde{p}}_i^{a\,*}(\mathbf{g}, z) f(\mathbf{g}, z) \equiv \langle\tilde{p}_i^a|\tilde{\Psi}\rangle. \quad (7)$$

B. Finite difference formulas

In order to solve Eq. (4), a uniform grid is constructed along the surface normal direction, as illustrated in Fig. 1. In order to stabilize the solution in the presence of exponentially growing solutions of Eq. (4), the uniform grid is further partitioned into sections $\sigma = 1, 2, \ldots \Sigma$, such that the last two points of an interior section is the same as the first two points of the next section:

$$z_{N-1}^{\sigma-1} = z_0^\sigma \quad \text{and} \quad z_N^{\sigma-1} = z_1^\sigma \quad \text{for } \sigma = 2 \cdots \Sigma. \quad (8)$$

The number of grid points in each section $(0, 1, 2, \ldots, N)$ should be roughly equal, but not necessarily identical. The numerical analysis involves solving the differential equation at each of the grid points $\{z_n^\sigma\}$ and satisfying boundary conditions at the two ends of the analysis region z_0^1, z_1^1 and $z_{N-1}^\Sigma, z_N^\Sigma$.

In this initial study, we are first concerned with investigating the stability of the basic algorithm. Therefore, we

make the simplifying assumption that all of the atomic spheres are fully contained between the initial (z_1^1) and final (z_N^Σ) end points of the evaluation region. Relaxation of this restriction causes more complicated indexing and will be considered in future work.

The solution of the differential equation (4) is approximated by a two-point recursion relation based on the Numerov method.[43] The wave functions coefficients on each grid point $f(\mathbf{g},z_n^\sigma)$ can be determined from a knowledge of their values at initial two points of each section according to an expression of the form:

$$f_n^\sigma = \sum_{\tau=1}^{\Sigma} (\mathbf{X}_{n0}^{\sigma\tau} f_0^\tau + \mathbf{X}_{n1}^{\sigma\tau} f_1^\tau), \tag{9}$$

where the $N_\mathbf{g}\times N_\mathbf{g}$ matrices $X_{n0}^{\sigma\tau}$ and $X_{n1}^{\sigma\tau}$ are given by Eq. (B11) in the Appendix, and where f_n^σ stands for the $N_\mathbf{g}$ coefficients $f(\mathbf{g},z)$, evaluated at the grid points $z=z_n^\sigma$. In order to evaluate Eq. (9), we must determine the values of the wave function at the interior partition boundaries (z_0^σ, z_1^σ for $\sigma=2\cdots\Sigma$) and at the exterior boundaries of the evaluation region (z_0^1, z_1^1) and ($z_{(N-1)}^\Sigma, z_N^\Sigma$). The interior matching conditions can be summarized by the following equations for $\sigma=2\cdots\Sigma$:

$$F_1^\sigma = F_N^{\sigma-1} = \sum_{\tau=1}^{\Sigma} \Xi^{\sigma\,\tau} F_1^\tau. \tag{10}$$

Here we have defined the $2N_\mathbf{g}$ vector of wave function coefficients at two consecutive points as

$$F_n^\tau \equiv \begin{pmatrix} f_{n-1}^\tau \\ f_n^\tau \end{pmatrix}, \tag{11}$$

while the $2N_\mathbf{g}\times 2N_\mathbf{g}$ composite matrix relating the beginning and end point of the partitions is given by

$$\Xi^{\sigma\,\tau} \equiv \begin{pmatrix} \mathbf{X}_{(N-1)\,0}^{\sigma\,\tau} & \mathbf{X}_{(N-1)\,1}^{\sigma\,\tau} \\ \mathbf{X}_{N\,0}^{\sigma\,\tau} & \mathbf{X}_{N\,1}^{\sigma\,\tau} \end{pmatrix}. \tag{12}$$

The corresponding relationship between the points on the outer boundaries takes the form:

$$F_N^\Sigma = \sum_{\tau=1}^{\Sigma} \Xi^{\Sigma\,\tau} F_1^\tau. \tag{13}$$

The determination of the surface wave function thus depends on the solution of the $2N_\mathbf{g}\Sigma$ equations (10) and (13). This has to be done with care so that the exponentially growing solutions of the differential equation do not numerically swamp the resultant wave function. Therefore, we can write these $2N_\mathbf{g}\Sigma$ equations as a single $2N_\mathbf{g}\Sigma\times 2N_\mathbf{g}\Sigma$ matrix equation in the form:

$$\mathcal{X}\mathcal{F} = \mathcal{G}, \tag{14}$$

where the matrix is given by

$$\mathcal{X} \equiv \begin{pmatrix} \Xi^{1\,1} & \Xi^{1\,2}-1 & \cdots & \Xi^{1\,\Sigma} \\ \Xi^{2\,1} & \Xi^{2\,2} & \cdots & \Xi^{2\,\Sigma} \\ \vdots & \vdots & \vdots & \vdots \\ \Xi^{(\Sigma-1)\,1} & \Xi^{(\Sigma-1)\,2} & \cdots & \Xi^{(\Sigma-1)\,\Sigma}-1 \\ \Xi^{\Sigma\,1} & \Xi^{\Sigma\,2} & \cdots & \Xi^{\Sigma\,\Sigma} \end{pmatrix}, \tag{15}$$

with the vector $\mathcal{F}$ representing the amplitudes at the initial points of each partition and the vector $\mathcal{G}$ representing the amplitudes at the end of the analysis region given by

$$\mathcal{F} = \begin{pmatrix} F_1^1 \\ F_1^2 \\ \vdots \\ F_1^\Sigma \end{pmatrix} \quad \text{and} \quad \mathcal{G} = \begin{pmatrix} 0 \\ 0 \\ \vdots \\ F_N^\Sigma \end{pmatrix}. \tag{16}$$

The composite equation (14) is now amenable to stable solution through the use of a singular value decomposition[33] of $\mathcal{X}$:

$$\mathcal{X} = \sum_s w_s U_s V_s^\dagger. \tag{17}$$

Here the real numbers w_s represents the "singular values," and U_s and $V_s^\dagger$ represent the corresponding column and row vectors, each of dimension $2N_\mathbf{g}\Sigma$. The matrix U formed from the U_s vectors is unitary as is the matrix V formed from the V_s vectors. For all the systems we have studied so far, we observe the distribution of singular values to have a very interesting structure. Namely, half of the singular values have the values $w_s>1$, while the other half have the values $w_s<1$. We have no explanation for this structure, but one suspects that it is related to the fact that the second order differential equation in general has exponentially growing and exponentially decaying solutions in equal proportion.

Since the vectors V_s span the solution space, we can generally write

$$\mathcal{F} = \sum_s V_s \langle V_s|\mathcal{F}\rangle. \tag{18}$$

This allows us to formally write the solution of Eq. (14) as

$$\mathcal{F} = \sum_s V_s \frac{\langle U_s|\mathcal{G}\rangle}{w_s}. \tag{19}$$

In practice, it will be important to control the effects of the very small singular values w_s which appear in the denominator of this expression. The corresponding relation between the outer boundary values is given by

$$F_1^1 = \sum_s V_s^1 \frac{\langle U_s^\Sigma|F_N^\Sigma\rangle}{w_s}, \tag{20}$$

where V_s^1 denotes the first $2N_\mathbf{g}$ components of the singular vector V_s and U_s^Σ denotes the last $2N_\mathbf{g}$ components of the singular vector U_s.

We are now ready to solve particular surface boundary value problems by specifying the appropriate conditions on the end values F_1^1 and F_N^Σ. The generalized Bloch conditions appropriate for analyzing the bulk material and the surface boundary conditions are described separately below.

C. Generalized Bloch boundary conditions

In this case, the analysis region represents the periodic repeat unit of the bulk system which we will denote as $c = z_N^{\Sigma} - z_1^1$. The corresponding generalized Bloch boundary condition for the wave function coefficients $f(\mathbf{g},z)$ takes the form

$$f_q(\mathbf{g},z+c) = e^{iqc} f_q(\mathbf{g},z), \tag{21}$$

where the surface wavevector q may be complex. For the discretization shown in Fig. 1, the Bloch condition applied to the two-point boundary functions at the beginning and end of the analysis region is given by

$$F_{Nq}^{\Sigma} = e^{iqc} F_{1q}^1. \tag{22}$$

Using this relation in Eq. (20), we can derive an eigenvalue relation for the wave function components F_1^1. The solutions of physical interest are those which correspond to propagating Bloch waves or those decaying within bulk region. Using the convention that the bulk material is in the region $z \to -\infty$ while the vacuum is in the region $z \to \infty$, this corresponds to surface wavevectors q with $\mathrm{Im}(q) \leqslant 0$. Using Eqs. (20) and (22), the generalized Bloch solutions can be written as a $2N_{\mathbf{g}} \times 2N_{\mathbf{g}}$ eigenvalue problem in the form

$$M^{\mathrm{B}} F_{1q}^1 = \lambda_q F_{1q}^1 \quad \text{with } \lambda_q = e^{-iqc}. \tag{23}$$

Each eigenvector F_{1q}^1 determines the $2N_{\mathbf{g}}$ components of initial wave function components and the matrix is given by

$$M^{\mathrm{B}} \equiv \sum_s \frac{1}{w_s} V_s^1 U_s^{\Sigma\dagger}, \tag{24}$$

where the small singular values are modified according to $w_s \to \min(w_s, \epsilon)$, where ϵ is an appropriate tolerance for small singular values. The small singular values ($w_s < \epsilon$) determine the eigenvalues λ_q which correspond to the wavevectors with $\mathrm{Im}(q) > 0$ and which are not needed for describing the physical wave functions in the current geometry. We will discuss appropriate choices for ϵ in Sec. IV A below.

Once the eigenvectors F_{1q}^1 are determined, the corresponding wave function coefficients $f_{n,q}^{\sigma}$ can be calculated from Eq. (9) using the initial values vector $\mathcal{F}_q$ evaluated from Eq. (19) which, in this case, can be written

$$\mathcal{F}_q = \sum_s V_s \frac{e^{iqc} \langle U_s^{\Sigma} | F_{1q}^1 \rangle}{w_s}. \tag{25}$$

The solutions of interest are those with generalized Bloch wavevectors q corresponding to waves propagating or decaying to the bulk solid ($\mathrm{Im}(q) \leqslant 0$). For convenience, the wave functions are all normalized to unity when integrated over the unit cell. The corresponding form for the PAW formalism is given by

$$\sum_{\mathbf{g}} \int_0^c dz |f_q(\mathbf{g},z)|^2 + \sum_{aij} \langle f_q | \tilde{p}_i^a \rangle O_{ij}^a \langle \tilde{p}_j^a | f_q \rangle = 1. \tag{26}$$

For propagating waves [$\mathrm{Im}(q)=0$] normalized in this way, the corresponding current along the surface normal is given by

$$J_q = \tilde{J}_q + \sum_{aij} \langle f_q | \tilde{p}_i^a \rangle J_{ij}^a \langle \tilde{p}_j^a | f_q \rangle, \tag{27}$$

where the smooth contribution is given by

$$\tilde{J}_q \equiv \frac{\hbar}{m} \int_0^c dz \, \mathrm{Im}\left(\sum_{\mathbf{g}} f_q^*(\mathbf{g},z) \frac{\partial}{\partial z} f_q(\mathbf{g},z) \right), \tag{28}$$

and the atom-centered contributions are given in terms of the all-electron $\phi_i^a(\mathbf{r})$ and pseudo $\tilde{\phi}_i^a(\mathbf{r})$ atomic basis functions

$$J_{ij}^a \equiv \frac{\hbar}{m} \int_{r \leqslant r_c^a} d^3 r \, \mathrm{Im}\left(\phi_i^{a*}(\mathbf{r}) \frac{\partial}{\partial z} \phi_j^a(\mathbf{r}) - \tilde{\phi}_i^{a*}(\mathbf{r}) \frac{\partial}{\partial z} \tilde{\phi}_j^a(\mathbf{r}) \right). \tag{29}$$

D. Semi-infinite boundary conditions

1. Continuum solutions

In this case, the analysis region represents the interface between the bulk material which exists in the region $z \leqslant z_1^1$ and the vacuum region which exists in the region $z \geqslant z_N^{\Sigma}$. For simplicity, we will restrict consideration to energies E below the vacuum level and thus to states which carry no net current. Extension of the analysis to the description of current-carrying states should be straightforward.

Since for $z \leqslant z_1^1$ the system is assumed to be identical to that of the bulk material, we expect the wave function to be described by a linear combination of propagating and decaying Bloch waves which can be written in the form:

$$f(\mathbf{g},z) = f_0(\mathbf{g},z) + \sum_p f_p(\mathbf{g},z) R_p + \sum_d f_d(\mathbf{g},z) D_d. \tag{30}$$

Here $f_0(\mathbf{g},z)$ represents a propagating Bloch wave with current $J_0 > 0$ (flowing from the bulk toward the vacuum region), $f_p(\mathbf{g},z)$ represents a propagating Bloch wave with current $J_p < 0$ (reflected from the surface), and $f_d(\mathbf{g},z)$ represents Bloch wave decaying into the bulk with wavevector $\mathrm{Im}(d) < 0$. The unknown coefficients $\{R_p\}$ and $\{D_d\}$ are to be determined. The corresponding expression for the boundary value F_1^1 vector is given by

$$F_1^1 = F_{10}^1 + \sum_p F_{1p}^1 R_p + \sum_d F_{1d}^1 D_d. \tag{31}$$

Since we are assuming that the solution has no net current, this constrains the reflection coefficients $\{R_p\}$ to satisfy the condition

$$J_0 + \sum_p J_p |R_p|^2 = 0, \tag{32}$$

where the current J_q in the surface normal direction is determined by Eq. (27).

In the vacuum region, we generally can write the wave function as a linear combination of $N_{\mathbf{g}}$ distinct solutions in the form

$$f(\mathbf{g},z)=\sum_{\mathbf{g}_0} f^{\mathrm{vac}}_{\mathbf{g}_0}(\mathbf{g},z)C^{\mathrm{vac}}_{\mathbf{g}_0} \quad \text{for } z \geqslant z^{\Sigma}_{\mathrm{N}}, \tag{33}$$

where the coefficients $\{C^{\mathrm{vac}}_{\mathbf{g}_0}\}$ need to be determined. An example of the form of $f^{\mathrm{vac}}_{\mathbf{g}_0}(\mathbf{g},z)$ is discussed in Appendix C.

The interface-vacuum boundary values then take the form

$$F^{\Sigma}_{N}=\sum_{\mathbf{g}_0} F^{\mathrm{vac}}_{\mathbf{g}_0}C^{\mathrm{vac}}_{\mathbf{g}_0} \equiv F^{\mathrm{vac}}C^{\mathrm{vac}}, \tag{34}$$

where the coefficients $\{C^{\mathrm{vac}}_{\mathbf{g}_0}\}$ are to be determined and the vector short hand notation is defined for convenience. This expression can be substituted into the right hand side of Eq. (20), while the left hand side should be given by the bulk form (31). In fact, Eq. (20) represents $2N_{\mathbf{g}}$ equations, which is larger than the number of unknown coefficients $\{R_p\},\{D_d\},\{C^{\mathrm{vac}}_{\mathbf{g}_0}\}$. In addition, we need to satisfy the constraint condition (32). Therefore, we choose to satisfy Eq. (20) in the least squares sense and to use a Lagrange multiplier to satisfy the current constraint (32). In preparing the least-squares equations, we note that the right hand side of Eq. (20) includes, in principle, the summation over all of the singular values w_s of the composite matrix $\mathcal{X}$. In this case, it is the small values of w_s which are important for the solution. Therefore, we rescale the expression in terms of the smallest singular value; $w_0 \equiv \min(w_s)$. It is then convenient to define a $2N_{\mathbf{g}}\times N_{\mathbf{g}}$ auxiliary matrix

$$M^{\mathrm{vac}} \equiv \sum_s \frac{w_0}{w_s} V^1_s \langle U^{\Sigma}_s | F^{\mathrm{vac}}\rangle. \tag{35}$$

In this expression, all of the singular values are included; for the smallest contributions $w_0/w_s \leqslant 1$ and for the problematic large singular values the contribution $w_0/w_s \ll 1$ will be negligible. In order to further stabilize the solution, we make another singular value decomposition on the matrix (35) which takes the form

$$M^{\mathrm{vac}}=\sum_t w^{\mathrm{vac}}_t U^{\mathrm{vac}}_t V^{\mathrm{vac}\dagger}_t. \tag{36}$$

Here the vectors V^{vac}_t have dimension $N_{\mathbf{g}}$ and span the space of the vacuum coefficients $\{C^{\mathrm{vac}}_{\mathbf{g}_0}\}$, while the vectors U^{vac}_t have dimension $2N_{\mathbf{g}}$ and span the space of boundary values F^1_1.

The χ^2 equation corresponding the boundary matching condition (20) then can be written

$$\chi^2=\left| F^1_{1\,0}+\sum_p F^1_{1\,p}R_p+\sum_d F^1_{1\,d}D_d-\sum_t U^{\mathrm{vac}}_t \tilde{C}^{\mathrm{vac}}_t \right|^2. \tag{37}$$

Here, the coefficients $\{\tilde{C}^{\mathrm{vac}}_t\}$ are related to the previously defined vacuum coefficients in Eq. (34) according to

$$C^{\mathrm{vac}}=\sum_t V^{\mathrm{vac}}_t \frac{w_0}{w^{\mathrm{vac}}_t}\tilde{C}^{\mathrm{vac}}_t. \tag{38}$$

The equations to minimize χ^2 with the current constraint (32) involve varying N_p reflection coefficients $\{R_p\}$, N_d decay coefficients $\{D_d\}$, and $N_{\mathbf{g}}$ vacuum solution coefficients $\{\tilde{C}^{\mathrm{vac}}_t\}$. It can be formulated as an iterative solution of a set of linear equations

$$M^C(\Lambda)X^C=X^C_0, \tag{39}$$

where the matrix $M^C(\Lambda)$ includes the Lagrange multiplier Λ in the form

$$M^C(\Lambda)=M^C_0+\Lambda J_p\delta_{pp'}. \tag{40}$$

Here M^C_0 is defined in Eq. (D1) and X^C_0 is defined in Eq. (D2). The solution vector is

$$X^C \equiv \begin{pmatrix} R_p \\ D_d \\ \tilde{C}^{\mathrm{vac}}_t \end{pmatrix}. \tag{41}$$

In each of these expressions, the indices p and p' represent N_p terms, the indices d and d' represent N_d terms, and t and t' represent $N_{\mathbf{g}}$ terms. The equations are solved for an initial value for the Lagrange multiplier (usually $\Lambda=0$) and then iterated to convergence using the increment

$$\Delta\Lambda=\frac{-(J_0+\sum_p J_p|R_p|^2)}{\sum_p 2Re(J_p\,\partial R^*_p/\partial\Lambda)}, \tag{42}$$

where $\partial R^*_p/\partial\Lambda$ is determined by taking the Λ derivative of the matrix equation (39). In the example system presented below, we find $\Lambda\approx 0$ for all the choices of E and κ considered.

Once the coefficients are determined, the interface wave function coefficients f^{σ}_n can be calculated from Eq. (9) using the initial values vector $\mathcal{F}$ given in Eq. (19) which can be calculated from

$$\mathcal{F}=\sum_s V_s \frac{w_0}{w_s}\sum_t \frac{\langle U^{\Sigma}_s|F^{\mathrm{vac}}V^{\mathrm{vac}}_t\rangle \tilde{C}^{\mathrm{vac}}_t}{w^{\mathrm{vac}}_t}. \tag{43}$$

2. Surface state solutions

This case is very similar to the continuum states considered above except that for the fact that there are no propagating Bloch states at a given surface wavevector κ and energy range, allowing for the possibility that new "surface" states which decay within the bulk material to exist in the surface region.

In this case, the wave function in the bulk region is expected to have the form

$$f(\mathbf{g},z)=\sum_d f_d(\mathbf{g},z)D_d, \tag{44}$$

using the same notation as Eq. (30). The corresponding expression for the boundary value vector F^1_1 is given by

$$F^1_1=\sum_d F^1_{1d}D_d, \tag{45}$$

The interface-vacuum matching condition is the same as in Eq. (34). Consequently, we can use the same analysis of the auxiliary matrix M^{vac} discussed above.

The χ^2 equation for the boundary matching condition is then given by

$$\chi^2 = \left| \sum_d F^1_{1\,d} D_d - \sum_t U^{\rm vac}_t \tilde{C}^{\rm vac}_t \right|^2. \quad (46)$$

In the surface case, the constraint we need to impose by using Lagrange multipliers comes from the wave function normalization condition

$$\sum_{\mathbf{g}} \int_{-\infty}^{\infty} dz |f(\mathbf{g},z)|^2 + \sum_{aij} \langle f|\bar{\tilde{p}}^a_i\rangle O^a_{ij} \langle \bar{\tilde{p}}^a_j|f\rangle = 1. \quad (47)$$

The equations to minimize χ^2 in Eq. (46) with the normalization constraint (47) can be expressed as a generalized eigenvalue problem:

$$M^S X^S_l = \lambda_l S X^S_l, \quad (48)$$

where the matrices M^S and S are given in Eqs. (E1) and (E2) and where the eigenvector X^S_l contains the coefficients

$$X^S_l = \begin{pmatrix} \{D_d\} \\ \{\tilde{C}^{\rm vac}_t\} \end{pmatrix}. \quad (49)$$

Since both the χ^2 and the normalization condition are bilinear forms, we have the very convenient result that for any given energy E and wavevector κ,

$$\min(\chi^2) = \lambda_0, \quad (50)$$

where λ_0 is the smallest eigenvalue of Eq. (48). A physical solution of the equations will correspond to $\min(\chi^2) < \epsilon_S$, where ϵ_S is a small tolerance which occurs at special energies indicating a surface state.

III. EXAMPLE SYSTEM—LI (110) WITH AND WITHOUT ADSORBED H

In order to test and evaluate the formalism, we have chosen to study the clean and hydrogenated Li (110) surface. This system has been studied by several authors both by experiment[44–46] and by simulation.[47–54] The experiments indicate that at low temperatures ($T \lesssim 160$ K) the clean Li (110) surface has no reconstruction and negligible relaxation. Sprunger and Plummer[44] showed at $T=160$ K, atomic H chemisorbs to form a "surface hydride." At higher temperatures the H diffuses into the bulk to form a bulk hydride. Quantum chemical techniques and cluster models have been used to simulate H adsorption on Li (110). These studies[47,48,54] indicate that the "bridge" position is the most stable adsorption site. Slab models have been used to study the work function of the Li (110) surface[49,50] and the formation of image potential states.[51,53,55]

The PAW functions used in this calculation were generated using the ATOMPAW code[38] with an $r_c=2.21$ bohr for Li ($2s$ $2p$ valence states) and $r_c=0.81$ bohr for H ($1s$ valence states). The exchange correlation functional was the local density approximations (LDA) of Perdew and Wang.[56] The bulk and slab results were generated using the PWPAW code.[39] The results for the generalized Bloch states and the interface and surface states were generated using the new code described in this paper. Brillouin zone integration was approximated with a uniform 16×16 sampling grid in the surface plane and equivalent sampling along the c axis for the bulk calculations. The zero of the energy scale for the results quoted in this section is taken to be that of the bulk Fermi level. The pseudowave functions were well-converged using the three-dimensional plane wave cutoff of $G_{\rm cut}=4$ bohr^{-1}. Equivalent convergence of the pseudo-wave functions was obtained in the surface geometry using the two-dimensional plane wave cut-off of $G_{\rm cut}=3$ bohr^{-1} and an integration step size of $h_z=0.224$ bohr.

A. Geometry

Since Li has the bcc structure, the repeat unit of the surface normal is $c=\sqrt{2}a$, where a denotes the cubic lattice constant (taken to be $a=6.337$ bohr.[57] It is convenient to choose the surface translation vectors to be

$$\mathbf{T}_1 = a\left(+\sqrt{\tfrac{1}{2}}\hat{\mathbf{x}} + \tfrac{1}{2}\hat{\mathbf{y}}\right)$$

$$\mathbf{T}_2 = a\left(-\sqrt{\tfrac{1}{2}}\hat{\mathbf{x}} + \tfrac{1}{2}\hat{\mathbf{y}}\right). \quad (51)$$

The surface reciprocal lattice vectors are given by

$$\mathbf{G}_1 = \frac{\pi}{a}\left(+\sqrt{\frac{1}{2}}\hat{\mathbf{x}} + \hat{\mathbf{y}}\right)$$

$$\mathbf{G}_2 = \frac{\pi}{a}\left(-\sqrt{\frac{1}{2}}\hat{\mathbf{x}} + \hat{\mathbf{y}}\right). \quad (52)$$

The Li atoms within a bulk unit cell are located at

$$\tau_1 = \tfrac{a}{4}(+\hat{\mathbf{y}} + \sqrt{2}\hat{\mathbf{z}})$$

$$\tau_2 = \tfrac{a}{4}(-\hat{\mathbf{y}} - \sqrt{2}\hat{\mathbf{z}}). \quad (53)$$

A projection of the surface geometry in the $y-z$ plane (also including the adsorbed H positions) is shown in the insert of Fig. 2.

B. Calculation of Bloch states

A simple test of the generalized Bloch formalism is to compare the band dispersions $E(\kappa,q)$ obtained from a three-dimensional band structure calculation with that obtained from Eq. (23) for special eigenvalues corresponding to $\mathrm{Im}(q)=0$. This is shown in Fig. 3 for κ at the $\bar{\Gamma}$ and $\bar{H}$ as indicated. The comparison is very good.

In order to get a more complete picture of the energy spectrum of our system including both bulk and surface effects, it is helpful to recognize that the wavevector in the surface normal direction q is no longer a good quantum number. It is, therefore, convenient to visualize the band structure projected into the surface Brillouin zone. That is, for each κ within the surface Brillouin zone, we plot all energies $E(\kappa)$ within the energy range

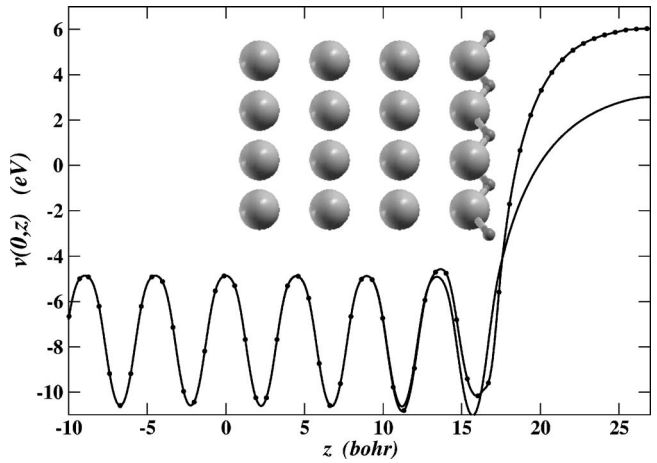

FIG. 2. Plot of the $\mathbf{g}=0$ component of the effective potential for the Li (110) interface with and without H adsorbate attached at the "bridge" sites (line with filled circles and plain line, respectively). For $z \geqslant 0$, the potentials were generated from self-consistent slab calculations, matched for $z \leqslant 0$ with the potential of the bulk material. The insert shows the geometry of the interface atoms projected in the $y-z$ plane, the Li atoms indicated with large spheres and the adsorbed H atoms indicated with small spheres.

$$E(\kappa,q_0) - \frac{\partial E(\kappa,q_0)}{\partial q}\delta q \leqslant E(\kappa) \leqslant E(\kappa,q_0) + \frac{\partial E(\kappa,q_0)}{\partial q}\delta q, \tag{54}$$

for a uniform grid of $0 \leqslant q_0 \leqslant \pi/c$, with δq chosen as the grid spacing, as shown in Fig. 4 along the $\bar{H}-\bar{\Gamma}-\bar{N}$ directions. The unshaded energy ranges of the diagram indicate where surface states can exist. These results are very similar to previous work of Chulkov and co-workers.[51]

C. Results obtained using slab supercell

Since, in the present work we are focusing on evaluating the properties of the method itself, we "cheat" and use the slab formalism to generate a self-consistent potential. This also allows us to make a direct comparison of the slab results with the results from our semi-infinite boundary formulation. The slab calculations were constructed with eight layers of Li and four vacuum layers. Since lattice relaxation has been found to be very small for this system[50] it was neglected in the present work. In addition to considering the pure material, we also considered H adsorption at the "bridge" site. The H atoms were placed at a height of 1.24 bohr from plane of the surface Li atoms, corresponding to a Li—H bond length of 3.01 bohr. This height for the H adsorbates was found to be approximately the most stable when the Li positions were held fixed the slab simulations. The $\mathbf{g}=0$ component of the effective potential for the Li (110) and Li (110)/H slabs (plain and decorated lines, respectively) are shown in Fig. 2 for $z \geqslant 0$. The calculated workfunction for ideal Li (110) is 3.0 eV, 10%–20% lower than earlier calculations.[49,50,59] With adsorbed H, in the assumed geometry, the work function increases to 6.0 eV.

The partial densities of states (weighted by the charge within each augmentation sphere) at the interior Li sites (full lines) and H sites (dashed line) for both the hydrogenated and ideal surface slab models are presented in Fig. 5. We see that the H contributions are in the continuum region of the spectrum ranging in energy from the bottom of the valence band to approximately −0.5 eV. In order to get a more detailed picture of the Li (110) and Li (110)/H surfaces in the slab models, we can also plot the energy bands of the slab which are shown in Fig. 6. The similarity between the slab spectrum and that of the projected surface bands shown in Fig. 4 is evident, although there are differences in the details. Comparing the spectrum the slabs with and without H, we see evidence of H-derived surface states at the boundaries of the surface Brillouin zone.

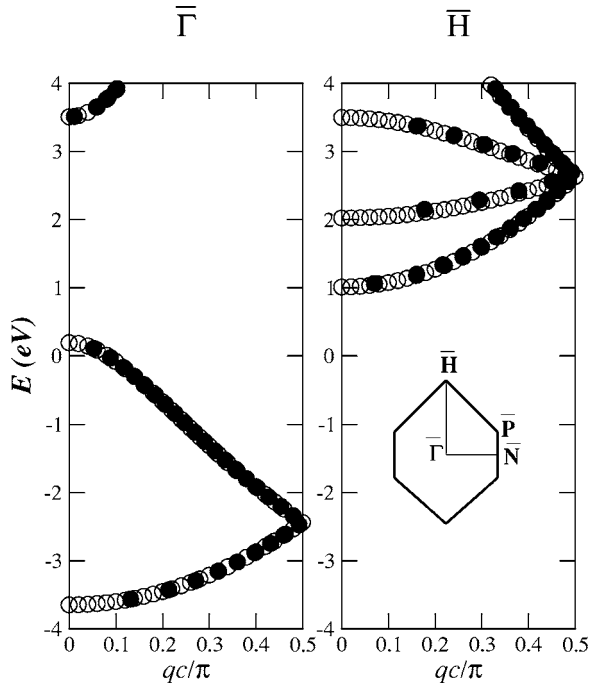

FIG. 3. Energy dispersion for propagating Bloch states as a function of surface wavevector q for two different values of κ as indicated. The empty circles indicate results obtained from the three-dimensional plane wave representation using the PWPAW code. The filled circles represent results obtained from Eq. (23). The insert shows a diagram of the surface Brillouin zone for the bcc (110) system (Ref. 58).

D. Continuum states with semi-infinite boundary conditions

The effective potential for the interface model was constructed from the results of the self-consistent slab and bulk calculations. Figure 2 shows the model potentials for $\mathbf{g}=\mathbf{0}$. We used the potential derived from four layers of the slab calculation for $z \geqslant 0$ and the bulk potential for $z \leqslant 0$. The zero of energy was adjusted so that the potential is continuous at $z=0$ and corresponds to the Fermi level of the bulk material. Using the formalism presented in Sec. II D 1, we can generate the pseudo-wave function components $f(\mathbf{g},z)$. Figure 7 shows plots of the pseudo-wave function densities $(\Sigma_{\mathbf{g}}|f(\mathbf{g},z)|^2)$ at the $\bar{\Gamma}$ point at various energies within the continuum range, comparing the effects of the ideal termina-

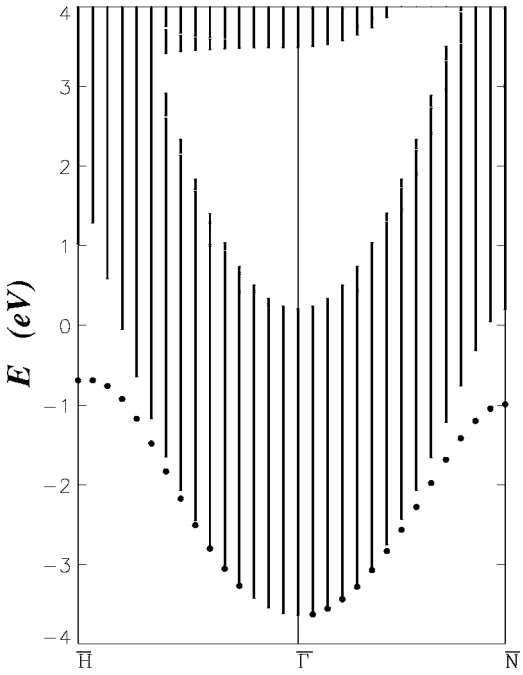

FIG. 4. Smear plot for bulk Li in the (110) surface geometry (vertical lines) obtained using Eq. (54). Also shown in this plot are H-induced surface states (filled circles) found for the Li (110)/H system.

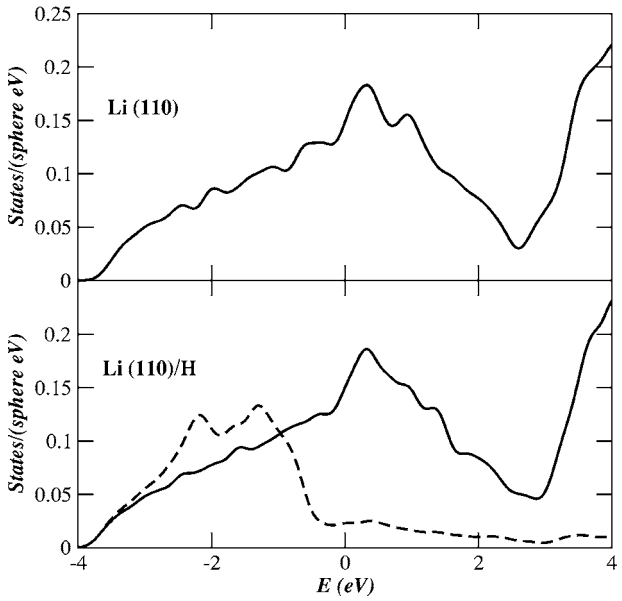

FIG. 5. Plot of the partial densities of states (DOS) for the eight-layer Li (110) and Li (110)/H slabs (upper and lower, respectively), calculated using a Gaussian broadening coefficient of 0.2 eV. The full lines represent the DOS weighted by the average charge within spheres at the interior Li sites, while the dashed line represents the DOS weighted by the average charge within spheres at the H sites.

tion with that of H adsorption. For this set of wave functions, we see that H has a quantitative but not qualitatively effect on the shape of the wave function density.[42] Not surprisingly, as energy increases the spatial modulation frequency also increases for these wave functions.

E. Surface states

Using the same model potentials (Fig. 2), we also searched for surface states outside the continuum region. Figure 8 shows a plot of the minimum χ^2 as a function of energy. The sharp minimum of the plot corresponds to a surface state. The χ^2 decreases at higher energies indicating the onset of the continuum at $E>0$.

For the ideal Li (110) surface, we found no surface states. Chulkov and co-workers[51] found surface states in the unoccupied band-gap near the $\bar{\Gamma}$ point in the presence of an image potential model. Our results suggest that these states do not exist in the absence of an image potential. In the presence of adsorbed H, we found surface states at the energies indicated in Fig. 4 in both the $\bar{H}-\bar{\Gamma}$ and $\bar{N}-\bar{\Gamma}$, directions. The H-induced surface states energies found in the semi-infinite analysis is shifted by approximately 0.3 eV relative to those found in the slab model (Fig. 6). Tests on larger slabs suggest that this energy shift is an indication that the interior of the eight-layer slab has not quite converged to a quantitative representation of bulk Li (110). By varying the integration step size and other calculational parameters, We estimate that the surface state energies within this model are determined within an error of approximately ±0.01 eV. Figure 9 shows the pseudo-wave function densities $(\Sigma_{\mathbf{g}}|f(\mathbf{g},z)|^2)$ for some of those surface states along the $\bar{N}-\bar{\Gamma}$, at the indicated energies. Not surprisingly, we see that the surface state at the $\bar{N}$ point at $E=-0.99$ eV is well-localized at near the surface-vacuum interface. For κ further toward the $\bar{\Gamma}$ point where the surface band becomes energetically closer the bulk bands, the surface wave functions increase their extension within the bulk of the crystal.

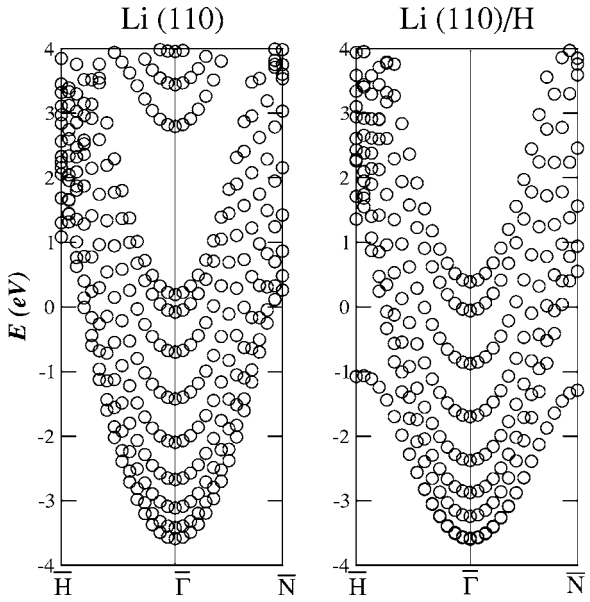

FIG. 6. Band structure diagram of eight-layer Li (110) slabs without (left) and with (right) adsorbed H.

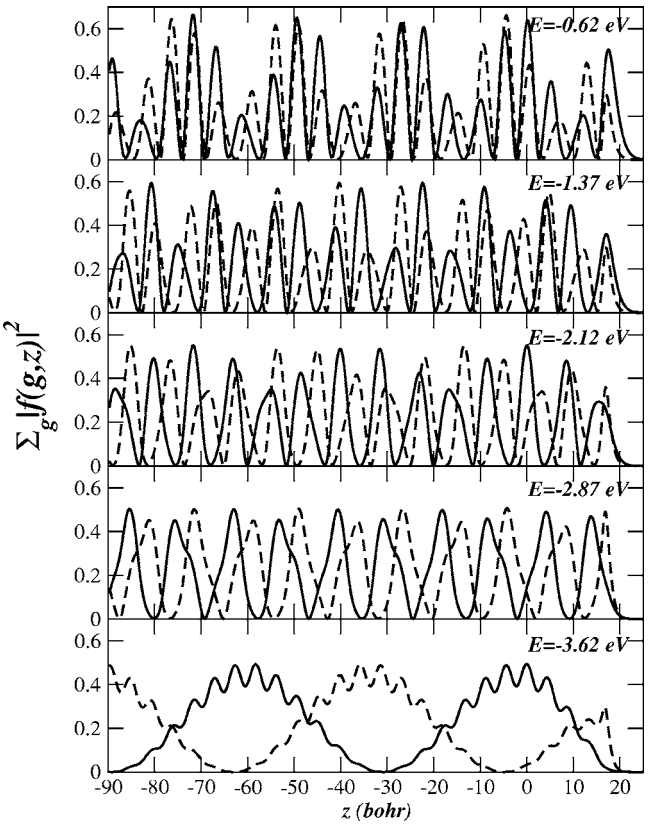

FIG. 7. Plot of the pseudo-wave function density in for Li (110) (full line) and Li (110)/H (dashed line) at various energies within the continuum spectrum at the $\bar{\Gamma}$ point.

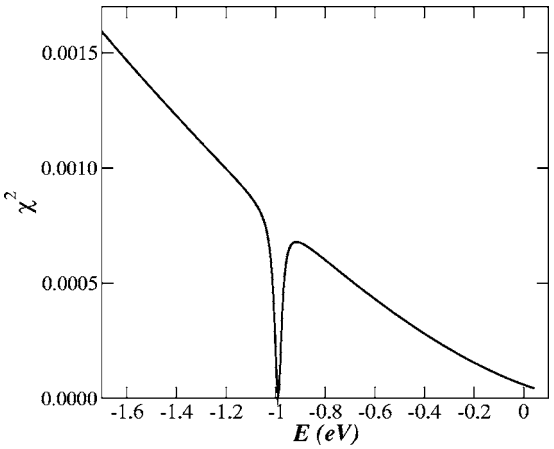

FIG. 8. Plot of $\chi^2=\lambda_0$ for Li (110)/H as a function of E at $\kappa=\bar{\mathrm{N}}$ showing a surface state at $E=-0.99$ eV and the bulk band edge at $E>0$ eV.

IV. DISCUSSION AND CONCLUSIONS

A. Sensitivity of results to calculational parameters

The results presented in Sec. III above were all obtained with $G_{\mathrm{cut}}=3$ bohr^{-1}, corresponding to $N_{\mathbf{g}}=19$ and $h_z=0.224$ or 0.112 bohr. The surface state energies shifted by 0.01 eV or less with the smaller step size. For the continuum solutions, the number of propagating waves for all states in the energy range considered was always $N_p=1$. The number of decaying waves N_d was chosen such that $0<\mathrm{Im}(q)\leqslant 10$ bohr^{-1} corresponding to $N_d\approx 4$. The number of partitions used in the calculation Σ was chosen as eight in the bulk region and 16 in the interface region which is roughly twice as large. The value of singular value cutoff for the generalized Bloch equations in Eq. (24) was chosen to be $\epsilon\approx 10^{-7}-10^{-10}$. Decreasing Σ by a factor of 2, decreasing h_z by a factor of 2 or increasing $G_{\mathrm{cut}}=4$ bohr^{-1}, each gave essentially the same results, showing that at least in this limited range, the formulation is quite stable. What changes in each of these cases is the distribution of the singular values $\{w_s\}$ as defined in Eq. (17). Using more partitions Σ or small step sizes h_z generally decreases the value of the maximum singular value w_s. However, in most of the cases, 3%–10% of the singular values w_s are smaller than machine precision and presumably their accuracy is uncontrolled. For the generalized Bloch solutions, these small singular values are filtered out of the analysis as explained above. However, for the interface solutions, this small singular values appear as a ratio w_0/w_s as defined in Eq. (35). While, by definition, $w_0/w_s\leqslant 1$, it is worrisome that these small values of w_s are not numerically well-defined. In fact, we find that the magnitudes of these singular values are not important so that we can reset all the small values to $w_s=\min(w_s,\epsilon)$. Apparently, what is important about these contributions is that the corresponding singular vectors V_s and U_s are rigorously orthogonal to those of the large singular values which contribute to the solution with a very much smaller weighting.

B. Further work to be done

While the results presented here are quite encouraging, further stability tests on more complicated structures will be needed to check the generality of the formalism. In addition, more analysis will be needed to include structures with augmentation spheres intersecting the boundaries of the analysis region. The complete formalism will also need to include self-consistency iterations which include the calculation of the interface charge density and the corresponding surface potential at each iteration, together with a scheme to stabilize the iterations. In addition, the entire method will need to be optimized for computational efficiency.

C. Summary

We have presented a stable scheme to calculate the electronic structure of surfaces and interfaces formulated as a semi-infinite boundary value problem. The method is based on the Numerov integration algorithm[43] and uses singular value decomposition[33] to control the exponentially growing contributions. The method is designed to work with the PAW formulation[36–39] of the Kohn-Sham equations, but can also be used with the soft-pseudopotential formulation of Vanderbilt[40] or with norm-conserving pseudopotentials approximated with separable nonlocal terms such as the form of Kleinman and Bylander.[41] The method has been successfully tested on the Li (110) surface with and without ad-

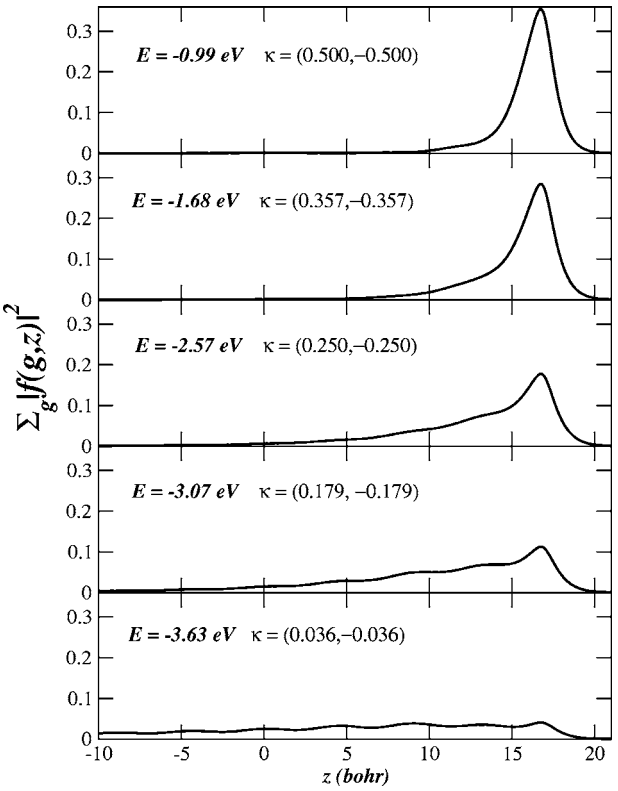

FIG. 9. Plot of the pseudo-wave function density for surface states for Li(110)/H along the $\bar{N}-\bar{\Gamma}$ direction of the surface Brillouin zone at the indicated energies and surface reciprocal lattice vectors [given in terms of fractions of the reciprocal lattice vectors listed in Eq. (52)].

sorbed H, showing both continuum and surface state wave functions. The results are very encouraging.

ACKNOWLEDGMENTS

This work was supported by NSF Grant No. DMR-0427055 and by Wake Forest University's DEAC high-performance computing facility. We would like to thank Professor V. Paúl Pauca for helpful discussions.

APPENDIX A: BASIC DEFINITIONS

The two-dimensional Fourier transform of the local potential in Eq. (5) is given an integral over the surface unit cell of the form

$$\bar{\tilde{v}}(\mathbf{g},z)=\frac{1}{\mathcal{A}}\int d^2r_\parallel e^{-i\mathbf{g}\cdot\mathbf{r}_\parallel}\tilde{v}(\mathbf{r}_\parallel,z). \tag{A1}$$

The two-dimensional Fourier transform of the projector function used in Eq. (5) is defined as

$$\bar{\tilde{p}}^a_i(\mathbf{g},z)\equiv\sqrt{\frac{1}{\mathcal{A}}}\int d^2r_\parallel e^{-i(\kappa+\mathbf{g})\cdot r_\parallel}\frac{\tilde{p}^a_{n_il_i}(|\mathbf{r}-\mathbf{R}^a|)}{|\mathbf{r}-\mathbf{R}^a|}Y_{l_im_i}(\widehat{\mathbf{r}-\mathbf{R}^a}), \tag{A2}$$

where $\tilde{p}^a_{n_il_i}(r)$ is the radial projector function such as determined in the ATOMPAW code,[38] and $Y_{l_im_i}(\hat{\mathbf{r}})$ is a spherical harmonic function. The integral can be evaluated using

$$\bar{\tilde{p}}^a_i(\mathbf{g},z)=\mathcal{N}^a_{l_im_i}(\kappa+\mathbf{g})\int_{|z-Z^a|}^{R^a_c}drp_{n_il_i}(r)P_{l_i}^{|m_i|}\left(\frac{z-Z^a}{r}\right)\times J_{|m_i|}(|\kappa+\mathbf{g}|\sqrt{r^2-(z-Z^a)^2}), \tag{A3}$$

where $P_{l_i}^{|m_i|}(u)$ represents an Associated Legendre function, $J_{|m_i|}(u)$ represents a Bessel function of integer order, and

$$\mathcal{N}^a_{l_im_i}(\kappa+\mathbf{g})\equiv e^{-i(\kappa+\mathbf{g})\cdot\mathbf{R}^a_\parallel}\left[\frac{(\kappa+\mathbf{g})_x}{|\kappa+\mathbf{g}|}+i\frac{(\kappa+\mathbf{g})_y}{|\kappa+\mathbf{g}|}\right]^{m_i}\times e^{-im_i\pi/2}\sqrt{\frac{\pi(2l_i+1)}{\mathcal{A}}}\sqrt{\frac{(l_i-|m_i|)!}{(l_i+|m_i|)!}}. \tag{A4}$$

APPENDIX B: FINITE DIFFERENCE FORMULAS

The Numerov algorithm involves terms from the local and nonlocal contributions of the equation. For the local contributions, the two-point recursion formula can be written in terms of $N_\mathbf{g}\times N_\mathbf{g}$ matrices:

$$\mathbf{C}^\sigma_{n\,r}=-(\mathbf{A}^\sigma_n)^{-1}(\mathbf{A}^\sigma_{n-2}\mathbf{C}^\sigma_{n-2\,r}+\mathbf{B}^\sigma_{n-1}\mathbf{C}^\sigma_{n-1\,r}), \tag{B1}$$

where $r=0$ or $r=1$, with special values:

$$\mathbf{C}^\sigma_{0\,0}=\mathbf{C}^\sigma_{1\,1}=\delta_{\mathbf{g},\mathbf{g}'},\quad \mathbf{C}^\sigma_{0\,1}=\mathbf{C}^\sigma_{1\,0}=0. \tag{B2}$$

Here,

$$\mathbf{A}^\sigma_n\equiv\mathbf{A}_{\mathbf{g},\mathbf{g}'}(z^\sigma_n)=\delta_{\mathbf{g}\mathbf{g}'}-\frac{h_z^2}{12}\mathcal{V}_{\mathbf{g}\mathbf{g}'}(z^\sigma_n) \tag{B3}$$

and

$$\mathbf{B}^\sigma_n\equiv\mathbf{B}_{\mathbf{g},\mathbf{g}'}(z^\sigma_n)=-2\delta_{\mathbf{g}\mathbf{g}'}-\frac{10h_z^2}{12}\mathcal{V}_{\mathbf{g}\mathbf{g}'}(z^\sigma_n). \tag{B4}$$

In these expressions, $\mathcal{V}_{\mathbf{g}\mathbf{g}'}(z^\sigma_n)$ has been defined in Eq. (5) and h_z denotes the uniform z mesh spacing.

The nonlocal terms involve a few more intermediate steps. First, for each atom site a and basis orbital index i, we can make the following recurrence relation for vectors of length $N_\mathbf{g}$

$$\mathcal{D}^a_i(z^\sigma_n)=(\mathbf{A}^\sigma_n)^{-1}[\mathcal{P}^a_i(z^\sigma_n)-\mathbf{A}^\sigma_{n-2}\mathcal{D}^a_i(z^\sigma_{n-2})-\mathbf{B}^\sigma_{n-1}\mathcal{D}^a_i(z^\sigma_{n-1})], \tag{B5}$$

where the $\mathbf{g}$th coefficient of $\mathcal{P}^a_i(z^\sigma_n)$ is given by

$$\mathcal{P}^a_{i\,\mathbf{g}}(z^\sigma_n)=\frac{h_z^2}{12}[\bar{\tilde{p}}^a_i(\mathbf{g},z^\sigma_{n-2})+10\bar{\tilde{p}}^a_i(\mathbf{g},z^\sigma_{n-1})+\bar{\tilde{p}}^a_i(\mathbf{g},z^\sigma_n)] \tag{B6}$$

with special values

$$\mathcal{P}^a_i(z^\sigma_0)=\mathcal{P}^a_i(z^\sigma_1)=\mathcal{D}^a_i(z^\sigma_0)=\mathcal{D}^a_i(z^\sigma_1)=0. \tag{B7}$$

The first two conditions follow from our simplifying assumption about the geometry of the system mentioned in

Sec. II B, while the second two are consistent boundary conditions. In order to evaluate the nonlocal coefficient (6), it is convenient to define the composite projector function

$$\bar{\tilde{q}}_i^a(\mathbf{g},z) \equiv \sum_j \frac{2m}{\hbar^2}(D_{ij}^a - EO_{ij}^a)(\bar{\tilde{p}}_j^a(\mathbf{g},z))^*, \tag{B8}$$

which, like $\bar{\tilde{p}}_i^a(\mathbf{g},z)$ is nonzero only in the region $Z^a - r_c^a \leqslant z \leqslant Z^a + r_c^a$. An atom-centered coupling matrix is determined by a piecewise continuous integration defined by

$$Z_{ij}^{ab} \equiv \sum_{\sigma=1}^{\Sigma} \int_{z_1^\sigma}^{z_N^\sigma} dz \sum_{\mathbf{g}} \bar{\tilde{q}}_i^a(\mathbf{g},z)\mathcal{D}_{j\,\mathbf{g}}^b(z), \tag{B9}$$

and an interaction term between the atom-centered and local contributions within the partition τ is defined by the following vector function in $\mathbf{g}$ space (with dimension $N_\mathbf{g}$):

$$Y_{j\,r\,\mathbf{g}}^{b\,\tau} \equiv \int_{z_1^\tau}^{z_N^\tau} dz \sum_{\mathbf{g}'} \bar{\tilde{q}}_j^b(\mathbf{g}',z)\mathbf{C}_{r\,\mathbf{g}'\mathbf{g}}^\tau(z). \tag{B10}$$

Here we have used the notation $\mathbf{C}_{r\,\mathbf{g}'\mathbf{g}}^\tau(z_n^\tau) \equiv \mathbf{C}_{n\,r,\mathbf{g}'\mathbf{g}}^\tau$. The integrals in Eqs. (B9) and (B10) are evaluated numerically using the uniform grid points $\{z_n^\tau\}$. In terms of these functions, the $N_\mathbf{g} \times N_\mathbf{g}$ matrix $\mathbf{X}_{nr}^{\sigma\tau}$ defined in Eq. (9) can then be written as

$$\mathbf{X}_{nr}^{\sigma\tau} = \mathbf{C}_{n\,r}^\sigma \delta_{\sigma\tau} + \sum_{ai\,bj} \mathcal{D}_i^a(z_n^\sigma)(I - Z)_{ai,bj}^{-1} Y_{j\,r}^{b\,\tau}. \tag{B11}$$

APPENDIX C: WAVEFORMS IN THE VACUUM REGION

In the vacuum region, $z > z_N^\Sigma$, we assume there are no atoms so that the potential is purely local. In general, there will be $N_\mathbf{g}$ distinct physical solutions corresponding to each reciprocal lattice vector which we label $\mathbf{g}_0$. In the present work, we consider the simpliest case, assuming that for $z \geqslant z_N^\Sigma$ the system is described by a constant potential

$$\bar{\tilde{v}}(\mathbf{g},z) = v_\infty \delta_{\mathbf{g},\mathbf{0}} \quad \text{for } z \geqslant z_N^\Sigma. \tag{C1}$$

The corresponding vacuum wave functions take the form

$$f_{\mathbf{g}_0}^{\text{vac}}(\mathbf{g},z) = \mathrm{e}^{-\kappa_{\mathbf{g}_0} z}\delta_{\mathbf{g}\mathbf{g}_0}, \tag{C2}$$

where

$$\kappa_{\mathbf{g}_0} \equiv \sqrt{|\kappa + \mathbf{g}_0|^2 + \frac{2m}{\hbar^2}(v_\infty - E)}, \tag{C3}$$

assuming that $E < v_\infty$. The form of $f_{\mathbf{g}_0}^{\text{vac}}(\mathbf{g},z)$ can easily be generalized to represent more complicated vacuum potentials such as those which contain image potential contributions.[51,53,55]

APPENDIX D: DETAILS OF CONTINUUM SOLUTIONS

The matrix and vector defined in Eq. (39) are defined as follows:

$$M_0^C \equiv \begin{pmatrix} +\langle F_{1p}^1|F_{1p'}^1\rangle & +\langle F_{1p}^1|F_{1d'}^1\rangle & -\langle F_{1p}^1|U_{t'}^{\text{vac}}\rangle \\ +\langle F_{1d}^1|F_{1p'}^1\rangle & +\langle F_{1d}^1|F_{1d'}^1\rangle & -\langle F_{1d}^1|U_{t'}^{\text{vac}}\rangle \\ -\langle U_t^{\text{vac}}|F_{1p'}^1\rangle & -\langle U_t^{\text{vac}}|F_{1d'}^1\rangle & +\langle U_t^{\text{vac}}|U_{t'}^{\text{vac}}\rangle \end{pmatrix}. \tag{D1}$$

The inhomogeneous term takes the form

$$X_0^C \equiv \begin{pmatrix} -\langle F_{1p}^1|F_{10}^1\rangle \\ -\langle F_{1d}^1|F_{10}^1\rangle \\ +\langle U_t^{\text{vac}}|F_{10}^1\rangle \end{pmatrix}. \tag{D2}$$

APPENDIX E: DETAILS OF SURFACE STATE SOLUTIONS

The matrices in Eq. (48) are defined as follows:

$$M^S \equiv \begin{pmatrix} +\langle F_{1d}^1|F_{1d'}^1\rangle & -\langle F_{1d}^1|U_{t'}^{\text{vac}}\rangle \\ -\langle U_t^{\text{vac}}|F_{1d'}^1\rangle & +\langle U_t^{\text{vac}}|U_{t'}^{\text{vac}}\rangle \end{pmatrix}. \tag{E1}$$

In this expression the braket notation is used to represent the inner product of the complex vectors $\{F_{1d}^1\}$ and $\{U_t^{\text{vac}}\}$ The overlap matrix takes the form

$$S \equiv \begin{pmatrix} \langle f_d|f_d'\rangle & 0 \\ 0 & \langle f_t|f_{t'}\rangle \end{pmatrix}. \tag{E2}$$

In this expression the braket notation is used to represent the integrals

$$\langle f_d|f_d'\rangle \equiv \int_{-\infty}^{z_1^1} dz \sum_{\mathbf{g}} f_d^*(\mathbf{g},z) f_{d'}(\mathbf{g},z) + \sum_{aij} \langle f_d|\bar{\tilde{p}}_i^a\rangle O_{ij}^a \langle \bar{\tilde{p}}_j^a|f_{d'}\rangle \tag{E3}$$

and

$$\langle f_t|f_{t'}\rangle \equiv \int_{z_1^1}^{\infty} dz \sum_{\mathbf{g}} f_t^*(\mathbf{g},z) f_{t'}(\mathbf{g},z) + \sum_{aij} \langle f_t|\bar{\tilde{p}}_i^a\rangle O_{ij}^a \langle \bar{\tilde{p}}_j^a|f_{t'}\rangle. \tag{E4}$$

In this expression, $f_t(\mathbf{g},z)$ is determined for $z_1^1 \leqslant z \leqslant z_N^\Sigma$ from Eq. (9) using the boundary value coefficients

$$\mathcal{F}_t = \sum_s V_s \frac{w_0}{w_s} \frac{\langle U_s^\Sigma|F^{\text{vac}}V_t^{\text{vac}}\rangle}{w_t^{\text{vac}}}, \tag{E5}$$

and for $z \geqslant z_N^\Sigma$, by

$$f_t(\mathbf{g},z) = \frac{w_0}{w_t^{\text{vac}}} \sum_{\mathbf{g}_0} f_{\mathbf{g}_0}^{\text{vac}}(\mathbf{g},z) V_{\mathbf{g}_0 t}^{\text{vac}}. \tag{E6}$$

*Corresponding author. Electronic mail: natalie@wfu.edu; http://www.wfu.edu/~natalie

[1] A. Zangwill, *Physics at Surfaces* (Cambridge University Press, Cambridge, 1988), ISBN 0-521-34752-1.
[2] M. Lannoo and P. Friedel, *Atomic and electronic sructure of surfaces* (Springer-Verlag, Berlin, 1991), ISBN 3-540-52682-X.
[3] H. Lüth, *Surfaces and Interfaces of Solid Materials*, 3rd ed. (Springer-Verlag, Berlin, 1995), ISBN 3-540-58576-1.
[4] K. Reuter, C. Stampfl, and M. Scheffler, in *Handbook of Materials Modeling, Part A. Methods*, edited by S. Yip (Springer, New York, 2005), ISBN-10 1-4020-3287-0.
[5] C. J. Fall, N. Binggeli, and A. Baldereschi, Phys. Rev. Lett. **88**, 156802 (2002).
[6] C. J. Fall, N. Binggeli, and A. Baldereschi, Phys. Rev. B **66**, 075405 (2002).
[7] L. -W. Wang, Phys. Rev. B **72**, 045417 (2005).
[8] N. D. Lang and W. Kohn, Phys. Rev. B **1**, 4555 (1970).
[9] N. D. Lang and W. Kohn, Phys. Rev. B **3**, 1215 (1971).
[10] N. D. Lang and A. R. Williams, Phys. Rev. Lett. **34**, 531 (1975).
[11] N. D. Lang and A. R. Williams, Phys. Rev. B **18**, 616 (1978).
[12] J. A. Appelbaum and D. R. Hamann, Phys. Rev. B **6**, 2166 (1972).
[13] J. A. Appelbaum and D. R. Hamann, Rev. Mod. Phys. **48**, 479 (1976).
[14] D. W. Jepsen, P. M. Marcus, and F. Jona, Phys. Rev. B **5**, 3933 (1972).
[15] J. B. Pendry, *Low Energy Electron Diffraction* (Academic, New York, 1974).
[16] D. W. Jepsen, Phys. Rev. B **22**, 5701 (1980).
[17] N. A. W. Holzwarth and M. J. G. Lee, Phys. Rev. B **18**, 5350 (1978).
[18] M. J. G. Lee and N. A. W. Holzwarth, Phys. Rev. B **18**, 5365 (1978).
[19] M. D. Stiles and D. R. Hamann, Phys. Rev. B **38**, 2021 (1988).
[20] M. D. Stiles and D. R. Hamann, Phys. Rev. B **40**, R1349 (1989).
[21] E. E. Krasovskii and W. Schattke, Phys. Rev. B **59**, R15609 (1999).
[22] E. E. Krasovskii, Phys. Rev. B **70**, 245322 (2004).
[23] W. Hummel and H. Bross, Phys. Rev. B **58**, 1620 (1998).
[24] D. Wortmann, H. Ishida, and S. Blügel, Phys. Rev. B **65**, 165103 (2002).
[25] P. Krüger and J. Pollmann, Physica B **172**, 155 (1991).
[26] J. Pollmann, P. Krüger, M. Rohlfing, M. Sabisch, and D. Vogel, Appl. Surf. Sci. **104-105**, 1 (1996).
[27] J. Pollmann and P. Krüger, Prog. Surf. Sci. **74**, 269 (2003).
[28] H. J. Choi and J. Ihm, Phys. Rev. B **59**, 2267 (1999).
[29] A. Smogunov, A. Dal Corso, and E. Tosatti, Phys. Rev. B **70**, 045417 (2004).
[30] P. Mavropoulos, N. Papanikolaou, and P. H. Dederichs, Phys. Rev. B **69**, 125104 (2002).
[31] H. Ishida, D. Wortmann, and T. Ohwaki, Phys. Rev. B **70**, 085409 (2004).
[32] P. A. Khomyakov and G. Brocks, Phys. Rev. B **70**, 195402 (2004).
[33] G. H. Golub and C. F. V. Loan, *Matrix Computations* (The Johns Hopkins University Press, 1983), ISBN 0-8018-3011-7, 0-8018-3010-9.
[34] P. Hohenberg and W. Kohn, Phys. Rev. **136**, B864 (1964).
[35] W. Kohn and L. J. Sham, Phys. Rev. **140**, A1133 (1965).
[36] P. E. Blöchl, Phys. Rev. B **50**, 17953 (1994).
[37] N. A. W. Holzwarth, G. E. Matthews, R. B. Dunning, A. R. Tackett, and Y. Zeng, Phys. Rev. B **55**, 2005 (1997).
[38] N. A. W. Holzwarth, A. R. Tackett, and G. E. Matthews, Comput. Phys. Commun. **135**, 329 (2001), available from the website http://pwpaw.wfu.edu.
[39] A. R. Tackett, N. A. W. Holzwarth, and G. E. Matthews, Comput. Phys. Commun. **135**, 348 (2001), available from the website http://pwpaw.wfu.edu.
[40] D. Vanderbilt, Phys. Rev. B **41**, R7892 (1990).
[41] L. Kleinman and D. M. Bylander, Phys. Rev. Lett. **48**, 1425 (1982).
[42] $\tilde{\Psi}_{\mu\kappa}(\mathbf{r}_\parallel)$ and $f_{\mu\kappa}(\mathbf{g},z)$ represent the pseudo-wave function. In the PAW method, the fully nodal wave functions and densities can be retrieved from a knowledge of this pseudo-wave functions. However only the pseudofunction results are presented in this paper.
[43] D. R. Hartree, *Numerical Analysis*, 2nd ed. (Oxford University Press, New York, 1958), pp. 142–143.
[44] P. T. Sprunger and W. E. Plummer, Surf. Sci. **307-309**, 118 (1994).
[45] D. M. Riffe and G. K. Wertheim, Phys. Rev. B **61**, 2302 (2000).
[46] S. C. Santucci, A. Goldoni, R. Larciprete, S. Lizzit, M. Bertolo, A. Baraldi, and C. Masciovecchio, Phys. Rev. Lett. **93**, 106105 (2004).
[47] H. O. Beckmann and J. Koutechký, Surf. Sci. **120**, 127 (1982).
[48] A. K. Ray and A. S. Hira, Phys. Rev. B **37**, 9943 (1988).
[49] K. Kokko, P. T. Salo, R. Laihia, and K. Mansikka, Phys. Rev. B **52**, 1536 (1995).
[50] K. Kokko, P. T. Salo, R. Laihia, and K. Mansikka, Surf. Sci. **348**, 168 (1996).
[51] E. V. Chulkov, V. M. Silkin, and P. M. Echenique, Surf. Sci. **391**, L1217 (1997).
[52] E. V. Chulkov, V. M. Silkin, and P. M. Echenique, Surf. Sci. **437**, 330 (1999).
[53] P. M. Echenique, J. M. Pitarke, E. V. Chulkov, and V. M. Silkin, J. Electron Spectrosc. Relat. Phenom. **126**, 163 (2002).
[54] I. Kara and N. Kosuz, J. Phys. Chem. Solids **63**, 861 (2002).
[55] E. V. Chulkov, J. Osma, I. Sarría, V. M. Silkin, and J. M. Pitarke, Surf. Sci. **433-435**, 882 (1999).
[56] J. P. Perdew and Y. Wang, Phys. Rev. B **45**, 13244 (1992).
[57] This was determined as the optimized lattice constant for the PAW functions used in the present work.
[58] E. W. Plummer and W. Eberhardt, in *Advances in Chemical Physics*, edited by I. Priogogine and S. A. Rice (Wiley, New York, 1983), Vol. 49, pp. 533–656.
[59] P. A. Serena, J. M. Soler, and N. García, Phys. Rev. B **37**, 8701 (1988).